

## Cleavage induced rows of missing atoms on ZnTe (110) surface

C. Çelebi, O. Ari, and R. T. Senger

*Department of Physics, Izmir Institute of Technology, 35430 Izmir, Turkey*

(Received 21 November 2012; revised manuscript received 17 January 2013; published 14 February 2013)

Cleavage induced rows of linear vacancy structures on *p*-doped ZnTe (110) surface are studied at room temperature by using cross-sectional scanning tunneling microscopy (X-STM). The oscillating contrast superimposed on the Te-driven occupied states neighboring to the vacancy cores are characterized at the atomic scale in order to determine the type of the missing component on the ZnTe surface matrix. We identify three major intensity distributions associated with different vacancy states. The X-STM images of three possible configurations comprising Zn only, Te only, and ZnTe binary vacancy structures on the ZnTe surface are modeled by using *ab initio* density functional theory calculations. The comparison of the X-STM measurements of each individual vacancy state to the corresponding theoretical simulation showed that unlike the Te vacancy, which leads to a local depression, the absence of Zn only or ZnTe binary gives rise to hillock features on the neighboring Te states of the ZnTe (110) cleaved surface. The theoretical STM images calculated for an undoped ZnTe crystal imply that possible doping-related effects on vacancy-induced features can be disregarded for interpreting the experimentally observed vacancy structures in our samples.

DOI: [10.1103/PhysRevB.87.085308](https://doi.org/10.1103/PhysRevB.87.085308)

PACS number(s): 68.37.Ef, 61.72.jd, 71.55.Gs, 31.15.A-

### I. INTRODUCTION

For more than a few decades, there has been a considerable amount of research effort carried out on the lattice imperfections including impurities, antisites, and vacancies in semiconducting materials. Scanning tunneling microscopy (STM), with its high spatial resolution and surface sensitivity, has now become a well-established method to investigate at the atomic scale the morphology and local electronic structure of those defects on and near the nonpolar (110) surface of III-V compounds.<sup>1-5</sup> Nevertheless, unlike widely studied III-V surfaces, there are only a few STM analyses so far on wide-gap II-VI materials despite their great technological importance. Following the first STM investigation of CdSe and CdS wurtzite crystals,<sup>6</sup> the measurements were done on the cross-sectional planes of ZnSe/BeTe and ZnSeTe/ZnTe multiple quantum wells.<sup>7-9</sup> As recently been determined by the cross-sectional STM (X-STM) technique, where the samples are necessarily cleaved in an ultrahigh vacuum (UHV) environment prior to measurements, the cleavage process was found to yield rows of missing atoms on the (110) surface of ZnTe substrates.<sup>9</sup> Since this peculiar effect has never been observed for III-V compounds, its origin was attributed to the structural differences between these two different types of semiconductors. In fact, the hardness and ionicity values of the two materials greatly differ from each other.<sup>10,11</sup> For example, in II-VI zinc-blende semiconductors with greater ionicity ( $0.5 < f_i < 0.7$ ) than III-V compounds, the bonding between group-II (cation) and group-VI (anion) components is weakened to a large extent.

It has been well established that the defects give rise to local distortions in the host atomic lattice depending on their charge state which can be determined with atomic resolution by STM measurements.<sup>12,13</sup> The distortions appear in the form of either local protrusions or depressions superimposed on the neighboring states and typically have a lateral extent of more than a few lattice constants. The polarity of the charge localized in the close vicinity of a vacancy center strongly depends on the type of the missing ion in the crystal lattice.

For example, a positively charged As vacancy on GaAs (110) surface leads to a local depression on the nearest neighbors,<sup>14</sup> whereas a negatively charged Ga vacancy gives rise to high-intensity hillock features<sup>15</sup> as observed in *occupied* state STM measurements. Nevertheless, there are still contradicting studies especially for the interpretation of the charge state associated with cation vacancies. It has been shown that a Ga vacancy in GaAs gives rise to a dark contrast superimposed on an array of  $3 \times 3$  missing *unoccupied* dangling bonds.<sup>16</sup> In a subsequent work, a dark X-shaped contrast consisting of one missing dangling bond has been attributed to the same Ga vacancy structure.<sup>17</sup> Recent theoretical calculations imply that the cation vacancies can be transformed into energetically more favorable and nonsymmetrically rebonded vacancy-antisite complex structures which may also appear as an anion vacancy in STM measurements.<sup>18</sup>

One of the main difficulties in experimentally determining the magnitude and polarity of the charge state is that the degree of the distortions shows a strong voltage bias dependence. Besides, the tip electronic state is usually unknown in a typical STM measurement. Hence, the interpretation of STM images can be quite complicated as in the evident case of missing Ga ion in GaAs. Nevertheless, advanced computational methods especially based on *ab initio* techniques made it possible to reproduce the experimentally obtained STM images of relaxed semiconductor surfaces over a range of sample-tip bias voltages.<sup>19,20</sup> A precise comparison of the measured results to theoretical simulations can be used to infer at the atomic scale the local electronic structure of the observed defects in semiconductor crystals.

### II. EXPERIMENTAL RESULTS AND DISCUSSION

X-STM measurements were performed on *p*-type phosphorous-doped ZnTe samples with a nominal doping concentration of about  $1 \times 10^{18} \text{ cm}^{-3}$ . Clean ZnTe (110) surfaces were obtained by cleaving the samples *in situ* inside an STM chamber with a base pressure of  $P < 2 \times 10^{-11}$  Torr.

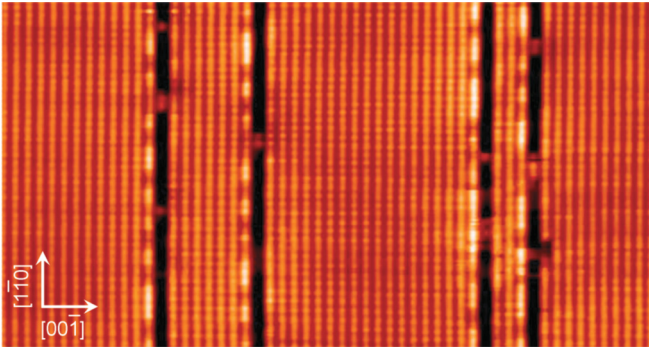


FIG. 1. (Color online) Large-area X-STM topography image taken from Ref. 9 of the ZnTe substrate ( $V_s = -3.5$  V,  $I_t = 50$  pA) comprising four monatomic wide rows of missing atoms on the (110) cleaved surface. The atomically resolved rows correspond to the Te sublattice of ZnTe. The frame size is  $30 \times 15$  nm<sup>2</sup>.

The topography measurements were carried out on the cleaved surfaces by using electrochemically etched polycrystalline tungsten tips that were further treated in vacuum as described in Ref. 21. The X-STM measurements were obtained at room temperature in constant-current ( $I_t = 50$  pA) scanning mode during which both topography and current images were recorded simultaneously. A large-area X-STM topography image of ZnTe (110) surface is shown in Fig. 1. The measurement was acquired with a tunnel voltage of  $V_s = -3.5$  V. At this sample bias range, where the Fermi level of the STM tip is moved far below the top of the valence band at  $k \approx 0$ , it becomes possible to image the Te-driven occupied states on ZnTe (110) surface. Unlike the III-V crystal surfaces, the application of a positive tunnel voltage gives rise to tip-induced modifications on our sample surface similar to those discussed in Ref. 9. In Fig. 1, the Te sublattice is well resolved together with perfectly ordered cleavage induced rows of missing atoms (denoted as vacancy lines) that were aligned parallel to each other. The observed vacancy lines preferentially lay along the  $[1\bar{1}0]$  direction and are perpendicular to the  $[00\bar{1}]$  or  $[00\bar{1}]$  direction. The observed linear vacancy structures give rise to a contrast consisting of basically two major components. The first part is the core of the vacancy row which is revealed as a dark line with a lateral dimension of approximately one occupied dangling-bond state. The second part is dominated by charge induced irregular corrugation along the nearest-neighbor Te states. Individual local traces seen along the  $[1\bar{1}0]/[\bar{1}10]$  axis of the vacancy line correspond to either Te or Zn atom which has not been removed during the cleavage process. Since the X-STM images directly represent the Te-driven occupied states, it may appear as if the vacancy lines are rows of missing Te atoms. However, after removing a single Te atom from the ZnTe surface matrix, the adjacent Zn atom is left behind with three available unoccupied dangling bonds, which is in fact energetically unfavorable. Therefore, it is most likely that aside from Te atoms, Zn atoms, and/or even ZnTe binaries are removed as well in the mechanical cleavage process. Our analyses from a series of subsequent measurements show that the observed vacancy structures are randomly separated from each other and have no lateral periodicity over the cleaved surface. An example of the tunnel voltage-dependent STM image of the Te rows next to the vacancy line is displayed in

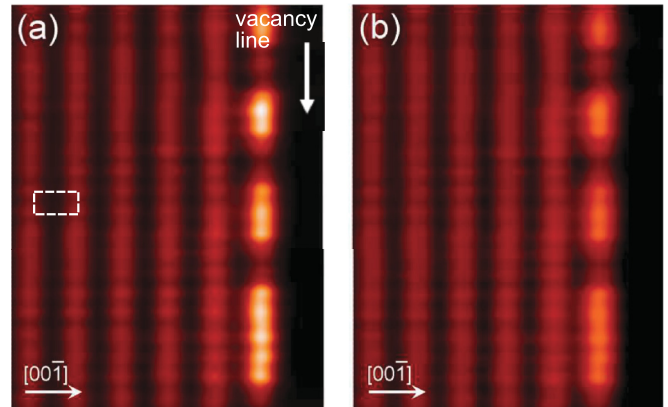


FIG. 2. (Color online) X-STM topography image of the Te sublattice on ZnTe (110) cleaved surface showing the voltage-dependent change of the vacancy-driven contrast for the Te states next to the vacancy line structure. The measurements were acquired at the tunnel setpoint of ( $V_s = -3.0$  V,  $I_t = 50$  pA) and ( $V_s = -3.5$  V,  $I_t = 50$  pA) for (a) and (b), respectively. Both of the images are in the same color scale range and have a frame size of  $4 \times 6$  nm<sup>2</sup>. Surface unit cell is indicated by a dashed box in (a).

Fig. 2. The apparent heights of the protrusions decrease when the tunnel voltage is increased [compare Figs. 2(a) and 2(b)]. This bias-voltage-dependent change of the height implies that the vacancy-induced features involving the nearest-neighbor Te states are more electronic than being topographic.

Figure 3(a) shows a high-resolution occupied state STM image of a single vacancy line on ZnTe (110) surface. The image was recorded at a relatively low sample voltage of  $V_s = -2.7$  V

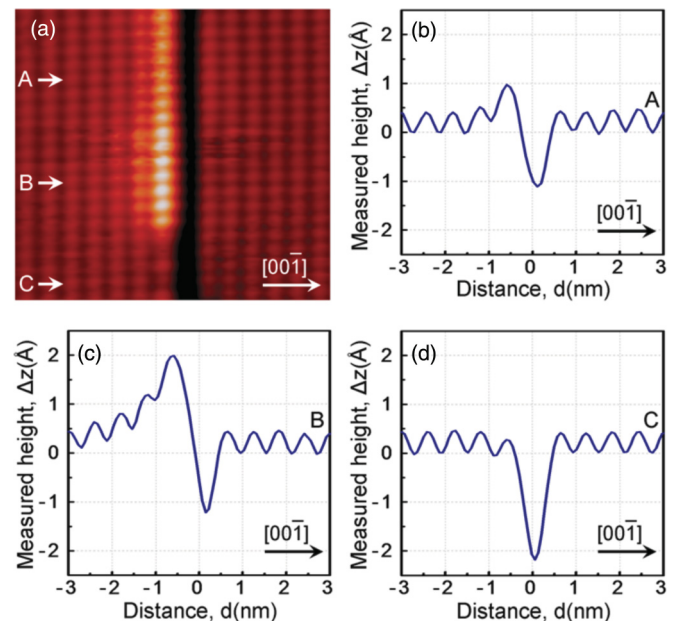


FIG. 3. (Color online) (a)  $8 \times 7$  nm<sup>2</sup> atomically resolved X-STM topography image of ZnTe (110) surface comprising a single vacancy line lying along the  $[1\bar{1}0]$  or  $[\bar{1}10]$  direction. The frame was acquired at the tunnel setpoint of ( $V_s = -2.7$  V,  $I_t = 50$  pA). An irregular contrast variation is seen along the nearest-neighbor Te rows. Panels (b), (c), and (d) display the corresponding topography line profiles measured along the arrows labeled with A, B, and C in (a).

to further enhance the contribution of the available electronic states to the tunneling. This region was specifically selected from the available STM data so that the most frequently observed contrast variations with different heights can be seen around an individual vacancy line in a single frame. Relative to the background Te sublattice, these contrast variations lie along the  $[1\bar{1}0]/[\bar{1}10]$  direction of the first neighboring Te row. The oscillating contrast, appearing as depression or elevation, in the STM images can be used to infer the polarity of the charges localized around the defect structures.<sup>21</sup> The polarity of the electrical charge localized in the adjacent states provides direct information for the type of the missing element in the ZnTe lattice. In order to quantitatively characterize the vacancy-driven height change in the neighboring Te rows, we applied individual line profiles along the directions shown with the arrows labeled as A, B, and C in Fig. 3(a). In accordance with those seen in the topography image, profile A and profile B exhibit vacancy-related missing dangling bonds and contrast variations involving the neighboring Te states in the  $[001]$  direction. Similar structures have already been observed in Zn-doped InP(110) and Si-doped GaAs (110) surfaces where their origin was attributed to dopant-vacancy complexes with atomic-scale dipoles.<sup>17,22</sup> Compared to the short-ranged abrupt elevation in profile A, the protrusion measured by profile B extends more than a few lattice constants along the  $[001]$  direction. The magnitude of the highest elevation superimposed on the nearest-neighbor Te state is measured to be about  $0.1 \pm 0.02$  nm in profile A, which is half the magnitude of the highest Te state in profile B. Those measurements show that the charges are strongly localized along the Te rows as determined from profile B. Unlike the two profiles, we identified in profile C a relatively weak local depression on the first neighboring Te state. The measured magnitude of the depression is about  $0.04 \pm 0.006$  nm, which is smaller than the intensity amplitude of the background Te sublattice ( $0.055 \pm 0.003$  nm). We found that the vacancy core characterized by profile C is deeper and broader than the vacancies determined by profiles A and B. The width of each missing dangling bond state is measured at the reference height ( $z = 0$ ) of the line-cut profiles which corresponds to the minima of Te sublattice corrugation away from the vacancy structure. The lateral width of the vacancy core in profile C was measured to be  $0.82 \pm 0.03$  nm which is approximately 50% larger than the lateral size of a single Te dangling bond state ( $0.56 \pm 0.01$  nm) on the ZnTe (110) surface. The core width in profile B was found to be  $0.53 \pm 0.04$  nm, whereas it reaches up to a value of  $0.65 \pm 0.03$  nm in profile A. Such a nonuniform lateral broadening (narrowing) of the vacancy core width is due to the apparent shrinkage (expansion) of the nearest-neighbor Te dangling bonds which is observed only at relatively low tunnel voltages. Similar lattice distortions were detected around the defect-induced states and their origin was attributed to possible electronic effects.<sup>23,24</sup> The electrons tunneling inelastically with sufficient energy can give rise to such lattice nonuniformities at relatively low sample voltages.

The interpretation of the observed vacancy-related depressions and elevations can be made within the framework of charge induced band bending effect. For example, for a positively charged vacancy,<sup>14</sup> surface bands bend downwards in the close vicinity of the vacancy core. This results in the

reduction of the number of states available for tunneling. Consequently, in constant-current mode topography measurements, the electronic feedback loop of the STM responds to this decreased number of states by reducing the tip-sample separation in order to maintain the constant current. The displacement of the tip towards the surface is reflected as local depression in the atomic lattice and is not related to the inward geometric movement of the neighboring dangling bond state.<sup>25</sup> It should be noted that the absence of anion component in various *p*-doped III-V materials with comparable electronic properties give rise to such apparent depressions in the nearest-neighbor dangling bond states.<sup>12,13</sup> In analogy, the local depression seen in the line-cut measurements (profile C) may also correspond to a positively charged missing Te state in the vacancy line. In the case of the elevations seen in profiles A and B, the corresponding vacancy cores may be associated with a negatively charged missing Zn state or even with a more complex structure such as atomic-scale dopant-vacancy dipole.

### III. THEORETICAL COMPARISON

In the experimental X-STM image shown in Fig. 3(a), three different height profiles are observed, which suggests that there are three different defect types occurring in the linear vacancy structure. In order to examine the underlying atomic and electronic structures of these defects, we considered the following defect types in theoretical simulations: Zn only, Te only, and ZnTe binary linear vacancies. Geometry optimizations and calculations of structural and electrical properties of the linear vacancies were performed using the SIESTA package<sup>26</sup> based on density functional theory (DFT).<sup>27</sup> We have used generalized gradient approximation (GGA) for the exchange and correlation potential as parametrized by Perdew, Burke, and Ernzerhof.<sup>28</sup> For geometry optimizations, a local relaxation has been performed using the conjugate gradient algorithm and the convergence criteria of  $0.04$  eV/Å and  $10^{-4}$  eV for the forces and total energies, respectively, in the self-consistency cycles. The electrostatic potentials were determined on a real-space grid with a mesh cutoff energy of 300 Ry. We make use of norm-conserving Troullier-Martins pseudopotentials<sup>29</sup> in the Kleinman-Bylander factorized form<sup>30</sup> and a double- $\zeta$  polarized basis set composed of numerical atomic orbitals of finite range. The Brillouin zone has been sampled with (3,15,1) points within the Monkhorst-Pack *k*-point sampling scheme. The optimized GGA value was used for the lattice constant and it was calculated to be  $6.0709$  Å for bulk ZnTe.

The surface calculations were performed using a seven-layer-thick slab which is terminated with pseudo-hydrogen atoms on one side. We used pseudo-hydrogen atoms with noninteger core charges to compensate for the presence of the artificial lower surface of the slab geometry: Zn and Te atoms of the lower surface were terminated by two types of hydrogenlike atoms with atomic numbers of 1.176 and 0.824, respectively, so that the valence charges of the Zn and Te ions retain their bulk values. During the geometry optimizations, the top four layers together with the pseudo-hydrogen atoms were allowed to relax fully, while layers five to seven were fixed at their bulk positions.



FIG. 4. (Color online) Two side views of the supercell used to simulate the (110) surface of ZnTe crystal. Lower surface of the slab is saturated by pseudo-hydrogen atoms to compensate effects of the artificial surface. During relaxation, lowest three layers of atoms are fixed at their bulk positions.

To avoid artificial interaction of the top and bottom surfaces of the slab construction, a  $10 \text{ \AA}$  vacuum region is added to the supercell in the perpendicular direction to the slab. In Fig. 4, the supercell used for surface simulations is shown. Linear vacancies are created by removing a single Zn or Te atom or a ZnTe binary from the topmost layer. Using the geometry-optimized structures, simulated STM images were then generated by using the Tersoff-Hamann method.<sup>31</sup> Partial charge density of the surface is calculated on a  $3 \text{ \AA}$  thick grid in real space which is located  $1 \text{ \AA}$  above the surface. The energy range from the Fermi level  $E_F$  to  $E_F + eV$  with an applied voltage  $V = -3 \text{ V}$  is used for LDOS integration to obtain the STM images. Fermi energies for Te-removed, Zn-removed, and ZnTe-binary removed cases are  $-2.67$ ,  $-2.91$ , and  $-2.66 \text{ eV}$ , respectively.

The calculated STM images of occupied-state ZnTe (110) surface are displayed in Fig. 5 for the three different linear vacancy configurations. Figure 5(a) corresponds to the case where a single row of Zn atoms is removed from the ZnTe (110) surface matrix. From our calculations, the absence of

Zn atoms was found to exhibit a pronounced nonsymmetric probability density profile with respect to the  $(\bar{1}\bar{1}0)$  mirror plane. The abrupt elevation along the neighboring occupied dangling bonds in the ZnTe [001] direction is due to the strong localization of the negative charge introduced by the missing Zn atom. Such accumulation of the negative charge induces a local upward band bending which is visible in the STM images as a bright contrast similar to that seen close to the vacancy structure labeled with A in Fig. 3. The atomic separation, as measured between the maximum of the two Te states neighboring to the vacancy, was found to be about  $0.66 \text{ nm}$ , which is also consistent with the experimentally obtained width ( $0.65 \pm 0.03 \text{ nm}$ ) of the vacancy feature in line profile A.

In contrast to missing Zn, the absence of Te component in the lattice creates a positively charged vacancy state. As seen in Fig. 5(b), the positive charge bound to the Te vacancy center gives rise to a pronounced depression on the nearest-neighboring Te states in the ZnTe [001] direction. It should be noted that earlier calculations predict such nonsymmetric structures related to the  $(+1e)$  charged anion vacancies to be lower in energy on the III-V (110) surfaces.<sup>32</sup> The depression found in the calculated image resembles that of the Te state characterized by profile C in Fig. 3. However, compared to the experimentally observed depression of the Te state in Fig. 3(d), the calculated one exhibits a relatively greater depression with respect to the background Te sublattice. Moreover, the lateral width of the calculated vacancy line is about a quarter of a lattice constant smaller than the width of the vacancy structure ( $\sim 0.82 \text{ nm}$ ) that was labeled with C in Fig. 3(a). In analogy to the theoretical result, it is most likely that the observed broadening of the vacancy structure in our experimental data is dominated by the neighboring Te atom with a reduced local density of states (LDOS), which was not resolved in our constant-current STM measurements. The weak Te-related signal at the vacancy line observed in the calculated profile does not show up in the corresponding experimental image [compare Fig. 5(b) with Fig. 3(c)] due to the low LDOS of the Te state. In other words, the STM tip does not discriminate

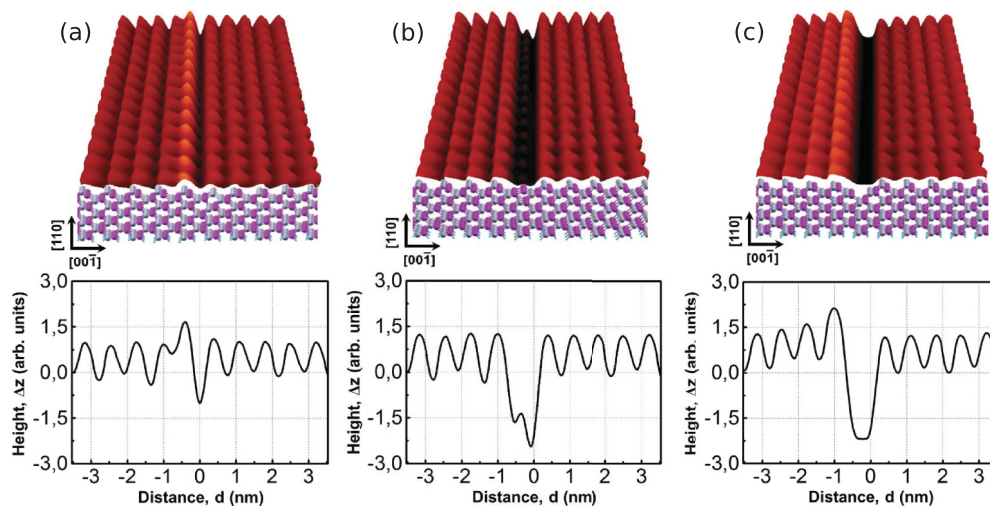


FIG. 5. (Color online) Simulated STM images comprising a single row of missing (a) Zn atom, (b) Te atom, and (c) ZnTe binary on a ZnTe (110) surface. Relaxed atomic structure of the corresponding simulation cell is given in each panel. The line profiles shown in (a), (b), and (c) can be compared with those presented in the panels (b), (d), and (c) of Fig. 3, respectively.

between the Te atom and the vacancy structure during the measurement.

The calculated probability density distribution for the missing row of ZnTe binary is shown in Fig. 5(c). The modeled ZnTe vacancy configuration also displays a nonsymmetric density profile with respect to the (110) plane of the defect line. In accordance with the X-STM image presented in Fig. 3(a) and with the line profile B [Fig. 3(c)], the calculations reveal a very similar large protrusion on the nearest-neighbor Te row whose contrast extends spatially over a few lattice constants with decreasing magnitude of height toward the [001] direction.

#### IV. CONCLUSIONS

The structural and electronic properties of the cleavage induced rows of missing atoms on ZnTe (110) surface are investigated at room temperature by cross-sectional scanning tunneling microscopy. The experimentally observed oscillating contrast appearing along the occupied Te states neighboring to the vacancy line structures is well reproduced by DFT calculations that were performed for an undoped ZnTe crystal. The vacancy structures associated with the missing Zn only, Te only, and ZnTe binary are interpreted by comparing their electronic contrasts with the corresponding theoretical STM simulations. We found that the negatively charged Zn

vacancy on the ZnTe (110) surface gives rise to an abrupt local protrusion on the first neighboring Te states, whereas a positively charged Te-related vacancy core creates a deep local depression. The spatial broadening of the vacancy line associated with the missing Te state has been attributed to the strongly reduced LDOS of the neighboring Te state which was not resolved in our STM measurements. In the case of ZnTe-binary-related vacancy structure, a long-range but decaying elevation was identified along the Te [001] sublattice direction. We should note that the simulation calculations suggest the asymmetric line-cut profiles seen in Zn and ZnTe vacancy lines to be not due to the structural surface reconstructions. Vertical deviations of topmost surface atoms after relaxation do not exceed 0.05 Å in any of the simulations. Thus, they reflect the electronic reconstruction in LDOS when the vacancies are introduced to the crystal surface. From the agreement between the theoretically obtained STM images and experimental results, it is concluded that possible doping-induced effects on the local electronic structure of vacancy-driven features can be disregarded for our samples with low doping level.

#### ACKNOWLEDGMENT

The authors would like to thank P. M. Koenraad from Eindhoven University of Technology for giving us the opportunity to perform X-STM experiments and for valuable discussions.

- 
- <sup>1</sup>J. F. Zheng, X. Liu, N. Newman, E. R. Weber, D. F. Ogletree, and M. Salmeron, *Phys. Rev. Lett.* **72**, 1490 (1994).
- <sup>2</sup>J. Gebauer, R. Krause-Rehberg, C. Domke, P. Ebert, and K. Urban, *Phys. Rev. Lett.* **79**, 958 (1997).
- <sup>3</sup>P. Ebert, *Appl. Phys. A* **75**, 101 (2002).
- <sup>4</sup>C. Çelebi, J. K. Garleff, A. Y. Silov, A. M. Yakunin, P. M. Koenraad, W. Van Roy, J.-M. Tang, and M. E. Flatté, *Phys. Rev. Lett.* **104**, 086404 (2010).
- <sup>5</sup>J. K. Garleff, A. P. Wijnheijmer, C. N. v. d. Enden, and P. M. Koenraad, *Phys. Rev. B* **84**, 075459 (2011).
- <sup>6</sup>B. Siemens, C. Domke, M. Heinrich, P. Ebert, and K. Urban, *Phys. Rev. B* **59**, 2995 (1999).
- <sup>7</sup>I. Yamakawa, Y. Akanuma, R. Akimoto, and A. Nakamura, *Appl. Phys. Lett.* **86**, 153112 (2005).
- <sup>8</sup>I. Yamakawa, Y. Akanuma, B. S. Li, R. Akimoto, and A. Nakamura, *Jpn. J. Appl. Phys.* **44**, L1337 (2005).
- <sup>9</sup>A. Wierst, J. M. Ulloa, C. Celebi, P. M. Koenraad, H. Boukari, L. Maingault, R. Andre, and H. Mariette, *Appl. Phys. Lett.* **91**, 161907 (2007).
- <sup>10</sup>I. Yonenaga and T. Suzuki, *Philos. Mag. Lett.* **82**, 535 (2002).
- <sup>11</sup>J. Alves, K. Watari, and A. Ferraz, *Solid State Commun.* **87**, 1001 (1993).
- <sup>12</sup>G. Lengel, R. Wilkins, G. Brown, M. Weimer, J. Gryck, and R. E. Allen, *Phys. Rev. Lett.* **72**, 836 (1994).
- <sup>13</sup>P. Ebert, K. Urban, and M. G. Lagally, *Phys. Rev. Lett.* **72**, 840 (1994).
- <sup>14</sup>K.-J. Chao, A. R. Smith, and C.-K. Shih, *Phys. Rev. B* **53**, 6935 (1996).
- <sup>15</sup>P. Ebert, X. Chen, M. Heinrich, M. Simon, K. Urban, and M. G. Lagally, *Phys. Rev. Lett.* **76**, 2089 (1996).
- <sup>16</sup>G. Lengel, R. Wilkins, G. Brown, and M. Weimer, in *Proceedings of the 20th Annual Conference on the Physics and Chemistry of Semiconductors Interfaces*, Vol. 11 (American Vacuum Society, Williamsburg, Virginia, 1993), p. 1472.
- <sup>17</sup>C. Domke, P. Ebert, M. Heinrich, and K. Urban, *Phys. Rev. B* **54**, 10288 (1996).
- <sup>18</sup>A. Höglund, S. Mirbt, C. W. M. Castleton, and M. Göthelid, *Phys. Rev. B* **78**, 155318 (2008).
- <sup>19</sup>H. Kim and J. R. Chelikowsky, *Phys. Rev. Lett.* **77**, 1063 (1996).
- <sup>20</sup>X. Duan, M. Peressi, and S. Baroni, *Phys. Rev. B* **72**, 085341 (2005).
- <sup>21</sup>C. Domke, M. Heinrich, P. Ebert, and K. Urban, *J. Vac. Sci. Technol. B* **16**, 2825 (1998).
- <sup>22</sup>P. Ebert, M. Heinrich, M. Simon, C. Domke, K. Urban, C. K. Shih, M. B. Webb, and M. G. Lagally, *Phys. Rev. B* **53**, 4580 (1996).
- <sup>23</sup>A. Richardella, D. Kitchen, and A. Yazdani, *Phys. Rev. B* **80**, 045318 (2009).
- <sup>24</sup>C. Çelebi, P. M. Koenraad, A. Y. Silov, W. Van Roy, A. M. Monakhov, J.-M. Tang, and M. E. Flatté, *Phys. Rev. B* **77**, 075328 (2008).
- <sup>25</sup>S. B. Zhang and A. Zunger, *Phys. Rev. Lett.* **77**, 119 (1996).
- <sup>26</sup>D. Sánchez-Portal, P. Ordejón, E. Artacho, and J. M. Soler, *Int. J. Quantum Chem.* **65**, 453 (1997).
- <sup>27</sup>W. Kohn and L. J. Sham, *Phys. Rev.* **140**, A1133 (1965).
- <sup>28</sup>J. P. Perdew, K. Burke, and M. Ernzerhof, *Phys. Rev. Lett.* **77**, 3865 (1996).
- <sup>29</sup>N. Troullier and J. L. Martins, *Phys. Rev. B* **43**, 1993 (1991).
- <sup>30</sup>L. Kleinman and D. M. Bylander, *Phys. Rev. Lett.* **48**, 1425 (1982).
- <sup>31</sup>J. Tersoff and D. R. Hamann, *Phys. Rev. B* **31**, 805 (1985).
- <sup>32</sup>P. Ebert, *Surf. Sci. Rep.* **33**, 121 (1999).